Title

Remote Sensing of Ground Deformation for Monitoring Groundwater Management Practices: Application to the Santa Clara Valley During the 2012–2015 California Drought

Journal

Journal of Geophysical Research: Solid Earth, 122(10)

ISSN

2169-9313

Authors

Chaussard, Estelle
Milillo, Pietro
Bürgmann, Roland
et al.

Publication Date

2017-10-01

DOI

10.1002/2017jb014676

Peer reviewed

Remote Sensing of Ground Deformation for Monitoring Groundwater Management Practices: Application to the Santa Clara Valley During the 2012–2015 California Drought

Estelle Chaussard[1], Pietro Milillo[2], Roland Bürgmann[3], Daniele Perissin[4], Eric J. Fielding[2], and Brett Baker[5]

[1] Department of Geology, State University of New York at Buffalo, Buffalo, NY, USA, [2] Jet Propulsion Laboratory, Pasadena, CA, USA, [3] Department of Earth and Planetary Science, University of California, Berkeley, CA, USA, [4] School of Civil Engineering, Purdue University, West Lafayette, IN, USA, [5] Santa Clara Valley Water District, San Jose, CA, USA

Correspondence to: E. Chaussard, estellec@buffalo.edu

Abstract

Groundwater management typically relies on water-level data and spatially limited deformation measurements. While interferometric synthetic aperture radar has been used to study hydrological deformation, its limited temporal sampling can lead to biases in rapidly changing systems. Here we use 2011–2017 COSMO-SkyMed data with revisit intervals as short as 1 day to study the response of the Santa Clara Valley (SCV) aquifer in California to the unprecedented 2012–2015 drought. Cross-correlation and independent component analyses of deformation time series enable tracking water through the aquifer system. The aquifer properties are derived prior to and during the drought to assess the success of water-resource management practices. Subsidence due to groundwater withdrawal dominates during 2011–2017, limited to the confined aquifer and west of the Silver Creek Fault, similar to predrought summer periods. Minimum water levels and elevations were reached in mid-2014, but thanks to intensive groundwater management efforts the basin started to rebound in late 2014, during the deepening drought. By 2017, water levels were back to their predrought levels, while elevations had not yet fully rebounded due to the delayed poroelastic response of aquitards and their large elastic compressibility. As water levels did not reach a new lowstand, the drought led to only elastic and recoverable changes in the SCV. The SCV lost 0.09 km^3 during the drought while seasonal variations amount to 0.02 km^3. Analysis of surface loads due to water mass changes in the aquifer system suggests that groundwater drawdowns could influence the stress on nearby faults.

1 Introduction

On 17 January 2014 California Governor, Jerry Brown, declared a drought state of emergency following the historically low surface water levels experienced across the state. The drought started in winter 2012 when precipitation dropped below historic averages and continued through 2015 with water resources more than 20% below average (Robeson, 2015). The drought, which is believed to have been caused by an offshore atmospheric

high-pressure system that redirected storms northward and away from California (Swain, 2015), posed significant challenges for water management (Costa-Cabral et al., 2016). When surface water levels are low, due to low snow, lake, and reservoir levels and reduced stream runoff, increased pressure is put on groundwater resources to satisfy urban, industrial, and agricultural needs. However, aquifer systems are fragile resources. If an aquifer system experiences a new record low in water levels, irreversible damage occurs to the system in the form of a permanent decrease in porosity and large land subsidence (Poland & Ireland, 1988; Wilson & Gorelick, 1996) as observed in the San Joaquin Valley (Farr, Jones, & Liu, 2016).

Using interferometric synthetic aperture radar (InSAR), land subsidence has been detected in many urban areas around the world, with consequences ranging from damage to infrastructure to increases in flooding in coastal areas (e.g., Chaussard et al., 2013; Chaussard, Wdowinski, et al., 2014; Galloway & Hoffmann, 2006). Groundwater extraction can lead to subsidence rates up to tens of centimeters per year (e.g., Bell et al., 2008), forcing implementation of controls on water extraction and artificial recharge (e.g., Shah, 2005). Subsidence can be due to elastic (recoverable) or inelastic (permanent) compaction with grain rearrangement if the hydraulic head drops below the previous lowest level (Poland & Ireland, 1988; Wilson & Gorelick, 1996). Both elastic and inelastic compaction lead to elevation changes proportional to variations in hydraulic head and to the thickness of the compacting layer.

Because of this relationship between ground deformation and water-level changes, monitoring of hydraulically induced deformation provides an opportunity for assessing and informing water management practices. Here we evaluate the changes associated with the California drought in the Santa Clara Valley (SCV) aquifer system. The SCV is located in the south of the San Francisco Bay Area, CA, near the city of San Jose and was the first area in the U.S. where subsidence due to groundwater withdrawal was recognized in the early 1900s (Galloway & Hoffmann, 2006; Tolman & Poland, 1940). Deformation prior to the 2012–2015 drought was studied by Schmidt and Burgmann (2003) (1992–2000) and by Chaussard, Burgmann, et al. (2014) (1992–2011). These works provide a basis for our analysis and enable comparison between typical deformation and drought-related deformation. While both of these studies relied on satellite-based deformation measurements with InSAR, which enables deformation mapping with a high spatial resolution, the data sets available during those periods had sparse temporal sampling (up to 35 day repeat but with often longer gaps). Such a limited temporal sampling leads to biases when interpreting rapidly changing systems, such as an aquifer system undergoing drought and recovery processes, and can affect the derived aquifer properties constrained from seasonal observations. Here we use the short revisit time of the Italian COSMO-SkyMed (CSK) synthetic aperture radar (SAR) constellation to study

the dynamic of the SCV aquifer over the period 2011–2017. This constellation relies on four satellites in different orbits, allowing for repeat intervals as short as 1 day during a 16 day cycle (Milillo, Riel, et al., 2016).

After introducing the Santa Clara Valley, we present the results of the 2011–2017 time series analysis, validate them with leveling data, and compare them with previous analyses. Second, we rely on the high spatial and temporal sampling of the InSAR analysis and on water well and extensometer data to analyze the effects of the drought on the SCV aquifer system. Third, we rely on cross-correlation and independent component analyses to characterize water dynamics and short-term spatiotemporal patterns embedded in the long-term time series. Fourth, we compare aquifer parameters retrieved from predrought analyses to aquifer parameters retrieved during the drought. Finally, we use water-level data and deformation measurements to estimate the surface load changes experienced by the SCV both in years with typical seasonal deformation and during the drought.

2 The Santa Clara Valley

The Santa Clara Valley (SCV), also known as Silicon Valley, is a shallow basin bounded by the Santa Cruz Mountains and San Andreas Fault to the west and the Diablo Range and Hayward-Calaveras fault zones to the east, in the San Francisco Bay Area. The nontectonically active Silver Creek Fault (SCF) cuts through the SCV and is responsible for the formation of the Evergreen pull-apart basin to the east (Wentworth et al., 2010). The Santa Clara Valley aquifer system is composed of a confined aquifer in the center, topped by a clay layer formed during the last interglacial sea level high stand ~125 ka (Koltermann & Gorelick, 1992), surrounded by an unconfined aquifer. The aquifer system is composed of up to 700 m thick compressible deposits of alternating marine clays (aquitards) and nonmarine sands (aquifer) resulting from successive changes in depositional environments in response to sea level fluctuations (Koltermann & Gorelick, 1992; Wilson & Gorelick, 1996). The Franciscan bedrock constitutes the base of the aquifer system, peaking through at a single location, the “Communication Hills.”

Between 1915 and 1965, water levels in the SCV declined by up to 60 m, leading to subsidence of up to 3.8 m and to flooding of large land areas (Tolman & Poland, 1940; Poland & Ireland, 1988). From 1965 to 1990, reduction in pumping and imported water from the Sierra Nevada halted the subsidence. Chaussard, Burgmann, et al. (2014) summarize the water-level change and deformation history of the valley between 1992 and 2011. Slow ground uplift dominated the 1992–2011 deformation near Sunnyvale (west of the SCF) and in the Evergreen Basin (east of SCF) with rates of ~4 mm/yr between 1992 and 2000 (Chaussard, Burgmann, et al., 2014; Schmidt & Burgmann, 2003). Between 2000 and 2011 only the Evergreen Basin (east of SCF) experienced continued uplift at ~1 mm/yr. The decrease in uplift rate in the Evergreen Basin, the cessation of uplift in the Sunnyvale area, and the

lack of agreement between this long-term deformation and water-level changes led Chaussard, Burgmann, et al. (2014) to conclude that this deformation resulted from the delayed poroelastic rebound of the aquifer system due to recovery of water levels after the 1960 lowstand.

Both Schmidt and Burgmann (2003) and Chaussard, Burgmann, et al. (2014) identified a strong seasonal signal present each year between 1992 and 2011, limited to the confined aquifer and west of the SCF with an amplitude of ~3 cm. Every winter, following precipitations, uplift of ~3 cm compensates the summer subsidence of similar amplitude and extent. The SCF sharply bounds the eastern extent of the seasonal deformation, acting as an effective barrier to across fluid flow, likely due to the presence of impermeable clay within the fault zone (Chaussard, Burgmann, et al., 2014).

Leveling, groundwater levels, and compaction from extensometers are used together with InSAR-derived ground deformation to characterize the effect of the drought on the SCV and evaluate the success of the water management practices used by the SCV water district to prevent the aquifer from reaching irreversible compaction.

3 The 2011–2017 Ground Deformation in the SCV

3.1 InSAR Data and Method

InSAR enables measurements of satellite-to-Earth-surface range change between subsequent flyovers of SAR spacecraft (or aircraft), assuming that the satellite orbits and topography are well removed (Burgmann, Rosen, & Fielding, 2000; Massonnet et al., 1993). We rely on 204 SAR images from the CSK satellites of the Italian Space Agency acquired between 2011 and 2017. CSK is a constellation of four X band satellites (9.6 GHz with a wavelength of 3.1 cm) and a mean incidence angle of 26.6° with repeat intervals as short as 1 day during a 16 day cycle. One ascending frame covers the SCV between 2011 and 2015 and two ascending frames between 2015 and 2017. Descending data are only available between 2013 and 2015. We remove the topographic phase component using a digital elevation model based on data from the Shuttle Radar Topography Mission (SRTM1 version 4; ~30 m, 1 arc sec) (Jarvis et al., 2008).

We integrate a large number of interferograms in a time series analysis with the SARPROZ software (Perissin, Wang, & Wang, 2011) to measure the time variable deformation and the SRTM height error. A multitemporal interferometric SAR (InSAR) approach (Milillo, Bürgmann, et al., 2016) extending the standard linear permanent scatterer (PS) technique (Ferretti, Prati, & Rocca, 2000, 2001) is used to solve for nonlinear motion with no a priori information (Colesanti et al., 2003). This modified PS technique provides a convenient method to measure time-dependent ground deformation with subcentimeter precision over large areas. We reference the displacement time series to a pixel that exhibits high coherence and is collocated with the Bay Area Regional Deformation network GPS station

LUTZ positioned on the bedrock of Communication Hills and showing minimal vertical motion (Figure 1) and use a temporal coherence threshold of 0.8. We extract the mean velocity map from nonlinear time series for each track and use ascending and descending data with overlapping time span (2013–2015) to decompose the signal in its vertical and east-west components (Wright, Parsons, & Lu, 2004).

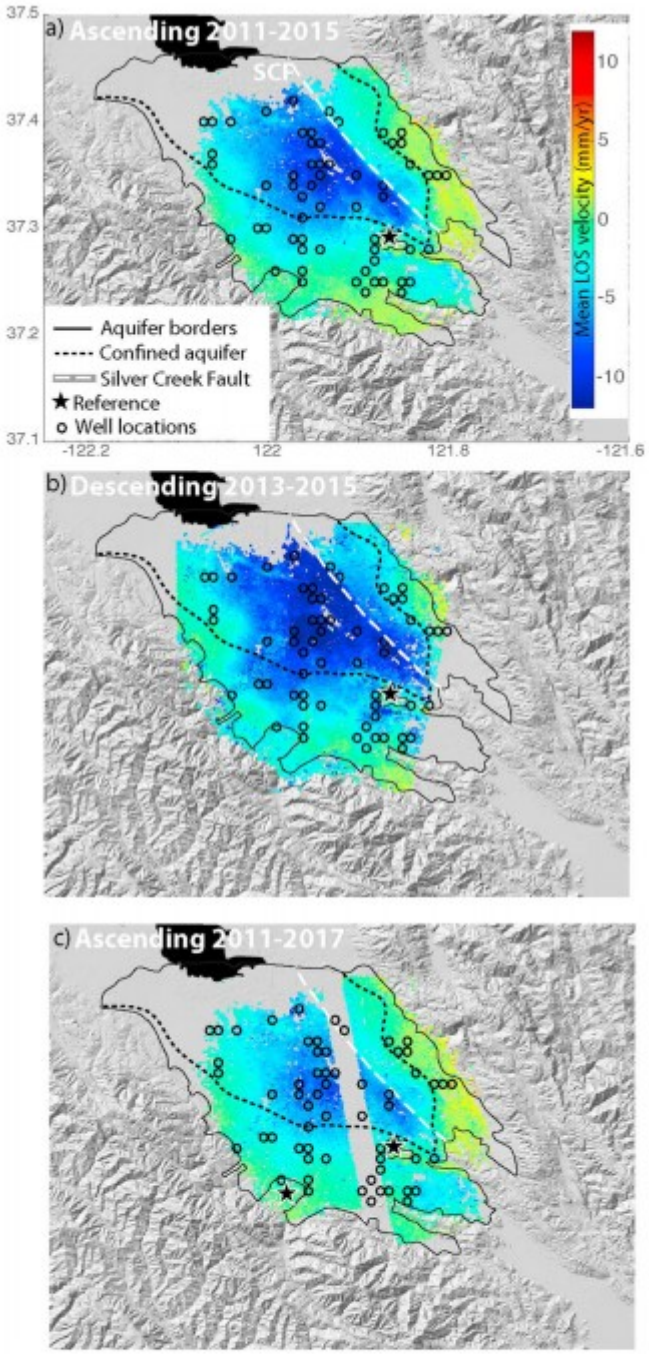

Figure 1. Mean LOS velocity maps from CSK over the Santa Clara Valley. (a) Ascending track from 2011 to mid-2015. (b) Descending track from 2013 to mid-2015. (c) Two separate ascending tracks showing data from 2011 to 2017. The black star shows the reference pixel located on bedrock. Only permanent scatterer pixels with a temporal coherence threshold above 0.8 are kept in the time series. Subsidence dominates during 2011–2017, with deformation mostly limited to the confined aquifer (dashed black line).

3.2 Ground Deformation and Water-Level Changes

Figure 1 shows the mean velocity maps for each frame, top: ascending frame with 2011–2015 data, middle: descending frame with 2013–2015 data, and bottom: ascending frames with combined 2011–2017 data. The vertical mean velocity map covering 2013–2015 (overlap of ascending and descending data) is shown in Figure 2. As previously noted by Chaussard, Burgmann, et al. (2014), most of the deformation in the basin is vertical. Therefore, we rely on the data set with the longest time span, the ascending 2011–2017 data (Figure 1, bottom), and assume that the observed deformation is vertical. The line of sight data are converted to vertical deformation considering the incidence angle of the satellite (e.g., Rosen et al., 2000). The gap in the data set is due to the fact that two neighboring frames of the CALIMAP CSK background acquisition campaign (Fielding et al., 2014) are used to cover the 2015–2017 time period. During 2011–2017, motion away from the satellite, i.e. land subsidence (Figure 1), is observed, which is limited to the confined aquifer and mostly west of the SCF.

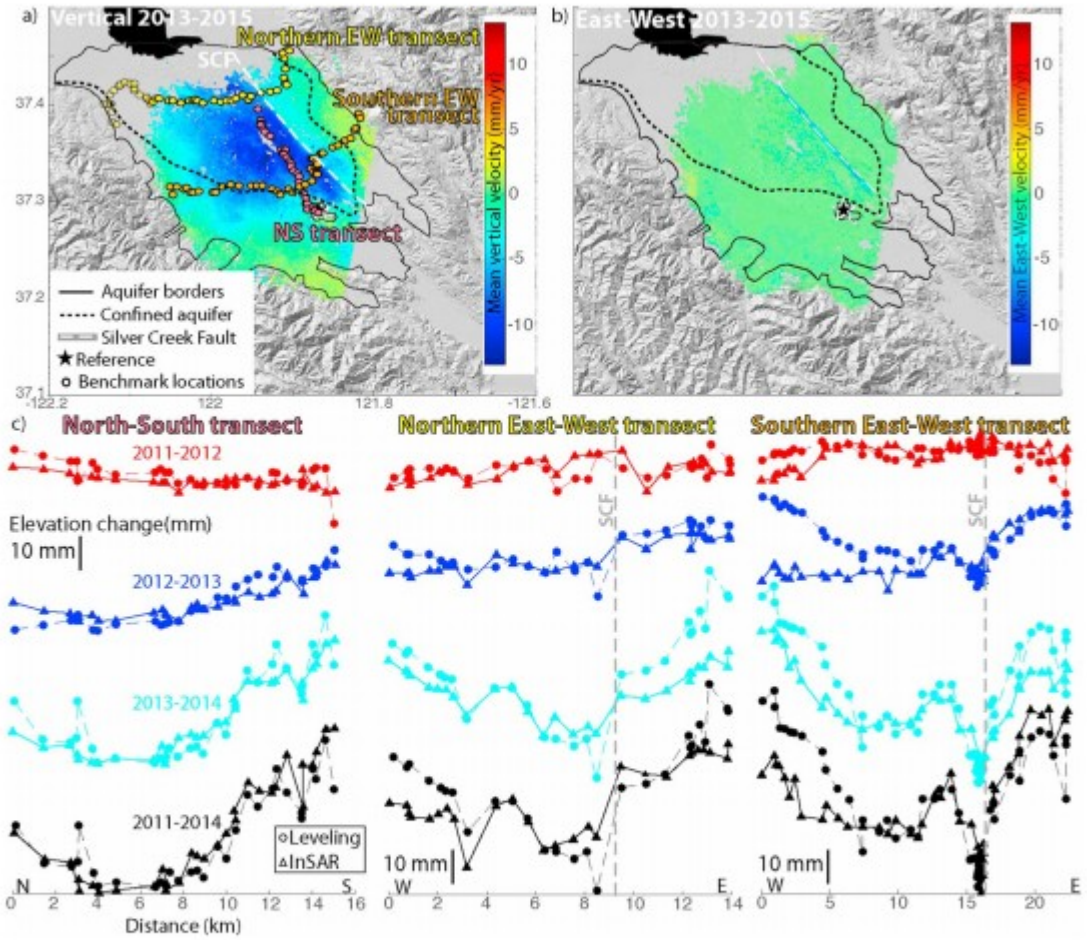

Figure 2. (a) Mean 2013–2015 vertical velocity map overlaid by the locations of benchmarks of the yearly leveling surveys. (b) Mean 2013–2015 east-west velocity map revealing only minimal near-SCF deformation. (c) Comparison between yearly leveling measurements (circles) along the three lines shown on the map (Figure 2a) and the corresponding vertical InSAR measurements (triangles) color coded by time span: red 2011–2012, blue 2012–2013, cyan 2013–2014, and black 2011–2014. The deformation measurements by the two methods agree well with each other, with a standard deviation of ~5 mm (within uncertainties of the methods), therefore validating the InSAR data.

We first validate these observations by comparing vertical deformation from InSAR with elevation changes measured along three leveling lines surveyed annually in September to November by the SCV water district (Figure 2). The yearly and total 2011–2014 deformation measured by the two methods agree well with a standard deviation of ~5 mm (Figure 2). Random error of leveling data accumulates with the square root distance from the reference point along the line with typical values of 1–2 mm/√km adding up to a maximum of 5 mm, while the InSAR uncertainties are on the order of 2–5 mm/yr based on comparison with GPS time series. Discrepancies between the InSAR and leveling observations are detected on the sides of the basin (Figure 2; east-west transects, 2012–2013, 2013–2014, 2011–2014), likely associated with accumulation of uncertainties in the leveling lines relative to the reference point in the center of the basin and the differences in measurement epochs. The subsidence in the confined aquifer and the sharp

deformation partitioning by the SCF are well resolved by both methods (Figure 2), therefore validating the InSAR time series results.

The observed subsidence during 2011–2017 represents a significant change from previous observations (Figure 3). Between 1992 and 2011 Chaussard, Burgmann, et al. (2014) detected mostly uplift, especially in the Evergreen Basin, east of the SCF (Figure 3c). The 2011–2017 net subsidence (Figure 3a) resembles the deformation observed seasonally each summer by Chaussard, Burgmann, et al. (2014) (Figure 3d) and Schmidt and Burgmann (2003). Similar seasonal deformation is also observed during 2011–2013 in our data set (Figure 3b). In such “normal” years, the summer subsidence (Figures 3b and 3d) is compensated by similar amplitude uplift in winter.

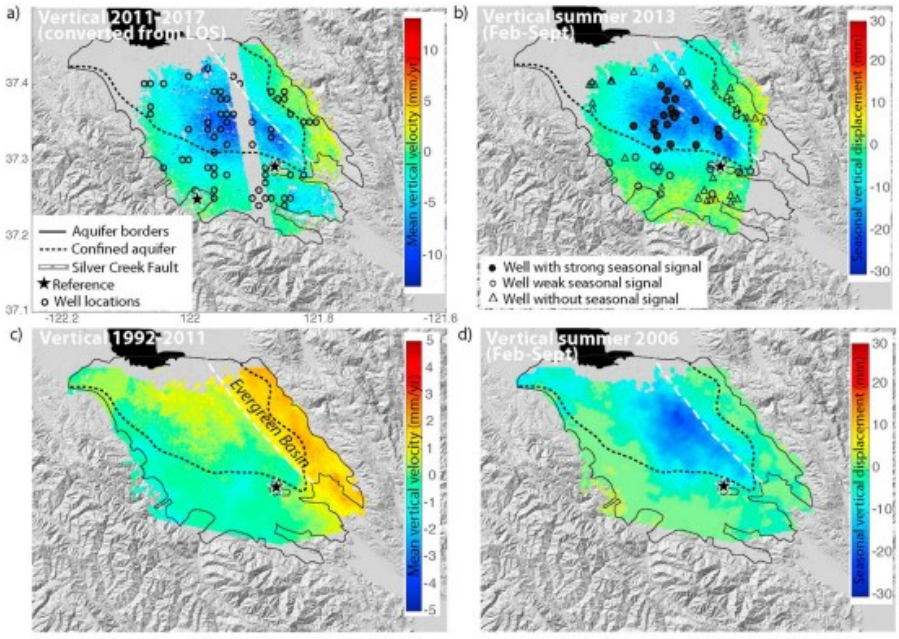

Figure 3. Comparison between velocity maps: (a) mean 2011–2017 vertical velocity map converted from the mean 2011–2017 LOS map shown in Figure 1c; (b) example of seasonal deformation observed in summer 2013 overlaid with the locations of wells experiencing strong seasonal changes (filled circles), of wells experiencing weak seasonal changes (black circles), and of wells experiencing no seasonal changes (triangles); (c) mean 1992–2011 vertical velocity map (Chaussard, Burgmann, et al. (2014)); and (d) example of seasonal deformation observed in summer of 2006 (Chaussard, Burgmann, et al., 2014). While the seasonal deformation observed during the 2011–2017 time span is of similar extent and magnitude as the seasonal deformation observed during 1992–2011 (Figures 3b and 3d), the long-term deformation has changed from uplift in 1992–2011 to subsidence in 2011–2017 (Figures 3a and 3c).

Figure 4 shows the time series of deformation and water well levels at two wells within the confined aquifer (Figures 4a and 4b) with extensometer data (SUNNY (Figure 4a), anchored to a depth of ~183 m, and MARTHA (Figure 4b), anchored to a depth of ~306 m) and at two wells in the unconfined aquifer (Figures 4c and 4d). The InSAR deformation (black triangles; Figure 4) agrees with the extensometer data (red), but the extensometers show lower amplitude deformation as they do not sample the entire thickness of the aquifer (total thickness near SUNNY ~250 m, total thickness near MARTHA ~350 m). In the northwest of the confined aquifer (Figure 4a) and in the unconfined aquifer (Figures 4c and 4d), the water levels (blue triangles)

show smaller fluctuations than in the center of the confined aquifer (Figure 4b).

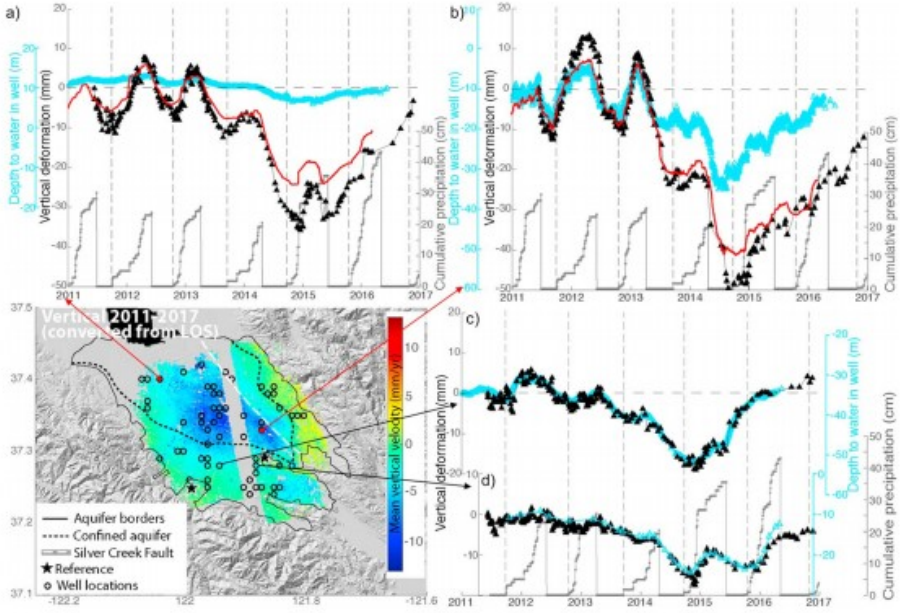

Figure 4. Comparison between 2011 and 2017 InSAR-derived ground deformation (black), compaction from extensometers (red), water-level changes (blue), and cumulative seasonal precipitation (gray; the last precipitation event is used to reset the cumulative year). (a and b) Examples for wells in the confined aquifer on the two different tracks and (c and d) examples for wells in the unconfined aquifer. The map in the bottom left corner shows the mean 2011–2017 vertical velocities (Figure 3a) and the well locations; arrows indicate the locations of the wells whose time series are shown in Figures 4a–4c.

Two years of typical seasonal deformation are observed between 2011 and mid-2013 (Figure 4). In winter, elevations and water levels rise following precipitation, and in summer similar amplitude subsidence is observed. In 2013, subsidence is observed until September and the onset of precipitation (Figure 4). Limited water-level rise and uplift are detected associated with small precipitations between September 2013 and February 2014. A significant drop in water levels and elevations is observed afterward until August 2014 (Figure 4). Minimum elevations and water levels are reached in summer (July and August) 2014 (Figure 4). In late 2014 (September), the water levels start rising 1 month in advance of the onset of significant precipitations due to water imports and conservation programs (Figure 4). Uplift starts with the precipitation in November and December 2014 (Figure 4). Water-level rise and uplift continues until 2017 with limited seasonal fluctuations. By the end of 2016 the water levels are back to their predrought levels, while the elevation is back to previous summer levels but has not yet fully recovered the drought-related subsidence.

4 Tracking Water Through the System

4.1 Cross-Correlation Analysis Between Water-Level Changes and Deformation

We rely on wells with daily water-level data and perform a cross-correlation analysis at each well to evaluate the time lag between water-level changes

and deformation in 2011–2014. Post-2014, as previously noted, the deformation lags behind well level changes as the system is no longer controlled by precipitation but by conservation and recharge efforts. The deformation observed by the CSK-InSAR time series has a temporal sampling of 1 to 8 days. Figure 5a shows the correlation between water levels and vertical surface displacements in 2011–2014. On average over the SCV, the deformation lags only 1 day behind changes in water levels. However, when tracking the time lag at individual wells, a spatial pattern is detected (Figure 5b). At wells in the unconfined aquifer and east of the SCF, the deformation and the water levels show no significant lag. In contrast, the time lag increases for wells in the confined aquifer, with a lag of 1 day for wells on the margins of the confined aquifer and a lag of up to 3 days for wells in the center (Figure 5b). Such a cross-correlation analysis with high temporal and spatial coverage therefore enables tracking water and deformation through the aquifer and highlights the system's dynamics and its properties.

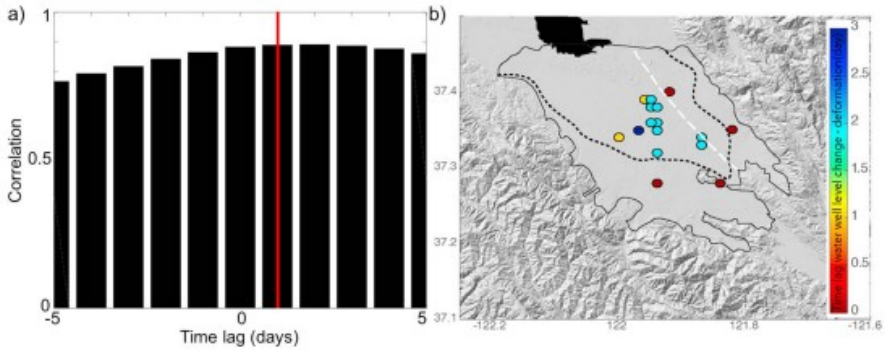

Figure 5. (a) Cross-correlation analysis between water-level changes and vertical surface displacements. On average the deformation is lagging 1 day behind the water-level changes at the scale of the basin. (b) Map of the time lags at individual wells showing that there is no lag in the unconfined aquifer and east of the SCF and an increased lag of up to 3 days for wells in the confined aquifer.

4.2 Independent Component Analysis Method

Independent component analysis (ICA) is a statistical and computational technique for separating independent sources linearly mixed in an output signal. For instance, when recording ground deformation, ICA can separate out noise embedded in the data and also deformation originating from different independent sources that are mixed together. ICA defines a generative model for the observed data, in which the observations are assumed to be a mixture of some unknown variables, and the mixing system is also unknown. The variables are assumed non-Gaussian and mutually independent and are called independent components (ICs). ICA can be seen as an extension of the principal component analysis (PCA) and factor analysis (Reimann et al., 2008). However, ICA is capable of finding the underlying sources when these methods fail (Hyvärinen, Karhunen, & Oja, 2004). ICA was introduced in the early 1980s to characterize a problem in the context of neural network modeling (Oja, 1982).

With a set of observations $x_1(t)$, x_2 (t), …, x_n (t) where each value of x corresponds to the deformation at a pixel (defined by its latitude and

longitude) and t the time of observations (varying from 1 to the number of SAR acquisitions) and assuming that these observations are generated as a linear mixture of independent components, we can write

$$\begin{pmatrix} x_1(t) \\ x_2(t) \\ \vdots \\ x_m(t) \end{pmatrix} = \mathbf{A} \begin{pmatrix} s_1(t) \\ s_2(t) \\ \vdots \\ s_n(t) \end{pmatrix}$$

where **A** is an unknown mixing matrix and $s_i(t)$ are the ICs. ICA consists of estimating both the matrix **A** and the $s_i(t)$, when we only observe the $x_i(t)$. The number of independent components s_n is equal to the number of hidden processes, which is not necessarily equal to the number of observations x_m. The goal of the ICA is to find a linear transformation by which the variables s_i are as independent as possible. Independence is a stronger property than uncorrelatedness used in a PCA, as independence implies nonlinear uncorrelatedness. For example, if s_1 and s_2 are independent, then the nonlinear transformations $g(s_1)$ and $h(s_2)$ are uncorrelated (their covariance is zero) (Hyvärinen et al., 2004). Independence relates to the central limit theorem which states that any linear mixture of independent random variables is more Gaussian than the original variables (Hyvärinen et al., 2004).

A first step in the ICA is to whiten the data to remove any correlations. The whitening process is simply a linear change of coordinate of the mixed data. Once the ICA solution is found in this “whitened” coordinate frame, we reproject the ICA solution back into the original coordinate system. The ICA is used to rotate the whitened matrix by minimizing the Gaussianity of the projection on all axes. Unlike in PCA, in ICA the axes do not have to remain orthogonal. By rotating the axis and minimizing Gaussianity, ICA is able to recover the original statistically independent sources (ICs). ICs correspond to the matrix that allows projecting the data in the initial space to one of the axis found by ICA. In this paper, we use the fixed-point algorithm called FastICA (Hyvärinen & Oja, **1997**) that has been tailored to exploit the non-Gaussianity for solving ICA.

From the preceding paragraphs, several properties of ICA can be deduced. First, ICA can only separate linearly mixed sources. Second, since ICA is dealing with clouds of points, changing the order in which the points are plotted has no effect on the outcome and the same applies for changing the component order. This is in contrast with the PCA method in which the index of a principal component relates to the percentage of variance explained. Third, since ICA separates sources by maximizing their non-Gaussianity, perfectly Gaussian sources cannot be separated. Finally, even when sources are not independent, ICA finds a space where they are maximally independent. In our application, ICA enables separating the observed time-dependent surface displacement history into a number of components with

distinct spatial and temporal patterns that relate to different underlying processes.

Our ICA considers 34,441 samples (pixels) per epoch and 204 epochs (SAR acquisition dates between 2011 and 2017). The number of ICs reflects the number of sources that contribute to the total observed deformation signal, when ignoring the noise sources. We consider that three ICs should be isolated based on the PCA results of Chaussard, Burgmann, et al. (**2014**) and based on the percentage of eigenvalues retained by the different components (Figure **6**a). We also examine additional components but find that the time series of eigenvectors for a fourth IC is highly variable and therefore unlikely to represent a real physical process of interest, and is likely associated with atmospheric noise (with high spatiotemporal variability). If more ICs are used than actual processes other independent components become biased because of the rule of independence. In the ICA with three components, the smallest number of (nonzero) eigenvalue retained is 330 and the largest is 6300, with 92.3% of the eigenvalues retained. In comparison, with four ICs, the component with the smallest number of eigenvalues retained is 131 and 93.9% of the eigenvalues are kept. Therefore, the addition of one component leads to only an increase of less than 2% in percentage of the eigenvalues retained, while in contrast, going from two to three components leads to an increase of over 4% of eigenvalues retained (88% versus 92.3%).

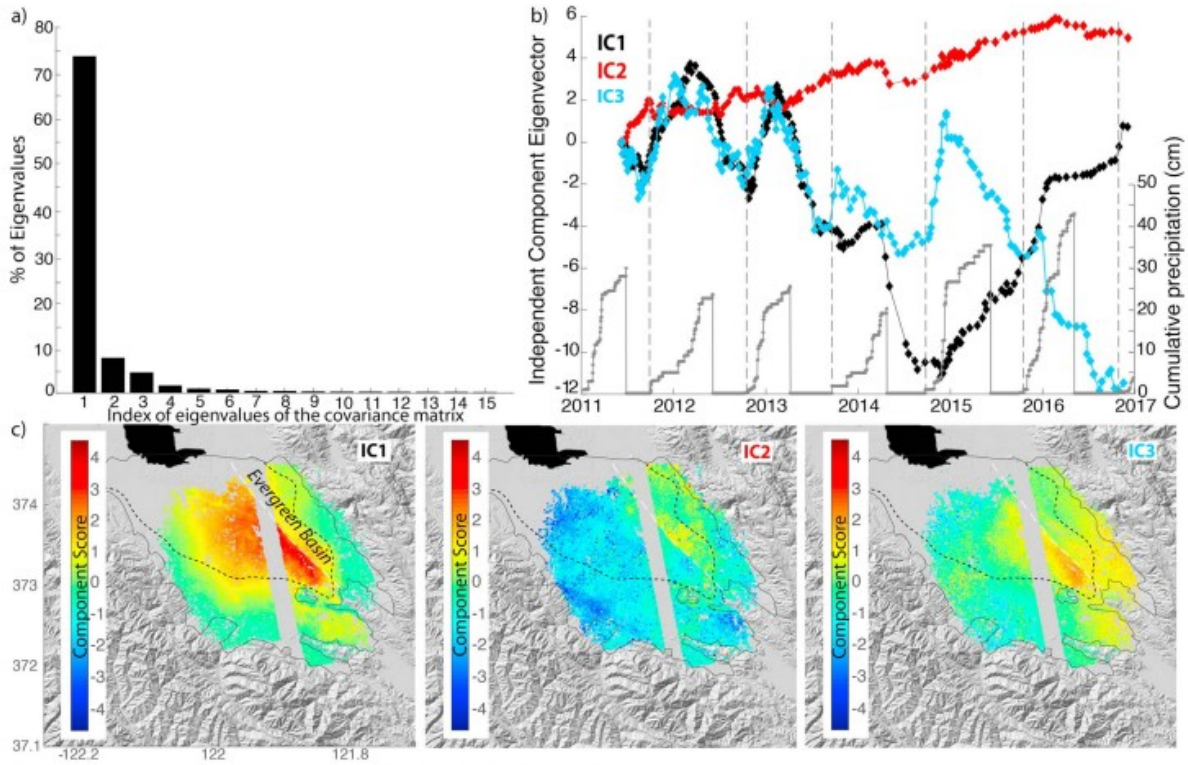

Figure 6. Independent component analysis on the 2011–2017 InSAR data set. (a) Eigenvalue plot. (b) Independent component eigenvectors. Gray dots show the cumulative precipitation reset after each wet season. (c) Maps of the independent component scores with score values rescaled so that multiplying the score by the eigenvector at each epoch provides the time-dependent vertical displacement (in mm) contributed by each component. IC1 shows mostly the long-term deformation previously described, IC2 shows the continuing uplift of the Evergreen Basin, and IC3 shows the deformation limited to the proximity of the SCF.

4.3 ICA Results

Figure 6 shows the results of the ICA with three components. The time series of eigenvectors shows when the signal is observed and the time-varying amplitude of the component (Figure 6b), while the map of the component's scores (Figure 6c) shows the spatial distribution of the signal from each component. The associated deformation history of each component can be recovered by multiplying the component score with its eigenvector at a given time taking into account the percentage of eigenvalues retained in the analysis (described above and applied here to the score axes). Positive score values correspond to uplift for positive eigenvector values and subsidence for negative eigenvectors.

The first component (IC1) has the same spatial extent and similar time series as observed in Figure 4 and therefore mostly represents the long-term deformation previously described. However, the sum of the components and of the noise left out by fixing the decomposition to three components is needed to fully recover the long-term deformation previously described. The second component (IC2) shows positive score values in the Evergreen Basin (east of the SCF) and always positive eigenvectors suggesting uplift of the Evergreen Basin between 2011 and 2017 at ~1 mm/yr. This uplift continues the 2000–2011 uplift detected by Chaussard, Burgmann, et al. (2014) at

similar rates. The third component (IC3) shows large positive scores near the southwest of the SCF with peaks in eigenvectors observed rapidly after precipitation, in advance of the peaks of IC1. This component suggests faster deformation near the SCF compared to the rest of the basin. While the extent of the IC3 score resembles the extent of the third principal component detected by Chaussard, Burgmann, et al. (2014) between 1992 and 2011, its temporal pattern is very different, with peaks occurring earlier than the mean seasonal peaks of deformation (IC1). This difference either reflects the bias in a PCA compared to an ICA associated with the forced orthogonality of the principal components or the lower temporal sampling (35 days maximum) of the 1992–2011 analysis. IC3 also shows positive scores of small amplitudes in parts of the Evergreen Basin, contributing to the net uplift together with IC2. IC1 and IC3 have positive correlation between 2011 and 2013, despite the time lag of the peaks, and become dissimilar (almost anticorrelated) in mid-2013. This change reflects that while the local deformation near the fault captured by IC3 remains controlled by precipitations, the deformation in the aquifer system captured by IC1 stop being regulated by precipitation during the drought (after mid-2013).

We additionally perform a cross-correlation analysis between the IC3 eigenvectors and the daily water-level data (Figure S1 in the supporting information). The time lag between water-level changes and the IC3 eigenvectors is of 0 day (Figure S1), whereas the lags between the SCV-wide deformation and the water level for these wells is of 2 days (Figure 5). This observation confirms that IC3 captures a faster response of deformation near the SCF than in the rest of the confined aquifer likely due to the properties of the fault zone discussed in section 7.

5 Aquifer Properties

We use the high temporal sampling of our data set to reevaluate the fundamental hydrological properties of the confined aquifer system obtained by Chaussard, Burgmann, et al. (2014), who relied on InSAR data during 1992–2011 with sparse temporal sampling. Figure 7a shows that the CSK temporal sampling allows for improved confidence in the confined aquifer storativity (S or Sk), estimated as the ratio of the deformation over the hydraulic head change (slope of the red line in Figure 7a and 7b) (e.g., Burbey, 2001; Freeze & Cherry, 1979; Helm, 1976; Hoffmann et al., 2001), and skeletal specific storage (Ssk). The storativity (S or Sk) corresponds to the volume of water taken into or released from storage per unit decline in hydraulic head, defined as the skeletal specific storage Ssk times the aquifer thickness in a confined aquifer. This method considers that water compressibility is negligible and that expansion and compression are only associated with the rock matrix (Chaussard, Burgmann et al., 2014). We perform three analyses of the Sk and Ssk values in the confined aquifer. First, we rely on the full-time span (2011–2017) of the CSK and well data; second, we split the data set in two periods, one with typical seasonal deformation (2011–2013.4) and one with “drought and recovery”

deformation (2013.4–2017). We compare these results to one another and compare these results to the 1992–2011 results of Chaussard, Burgmann et al. (2014). While small variations in the Sk and Ssk values are expected due to the improved sampling of the deformation data, changes in properties by an order of magnitude or more in the 2013.4–2017 data set would suggest inelastic deformation and permanent decrease in porosity of the aquifer due to the drought.

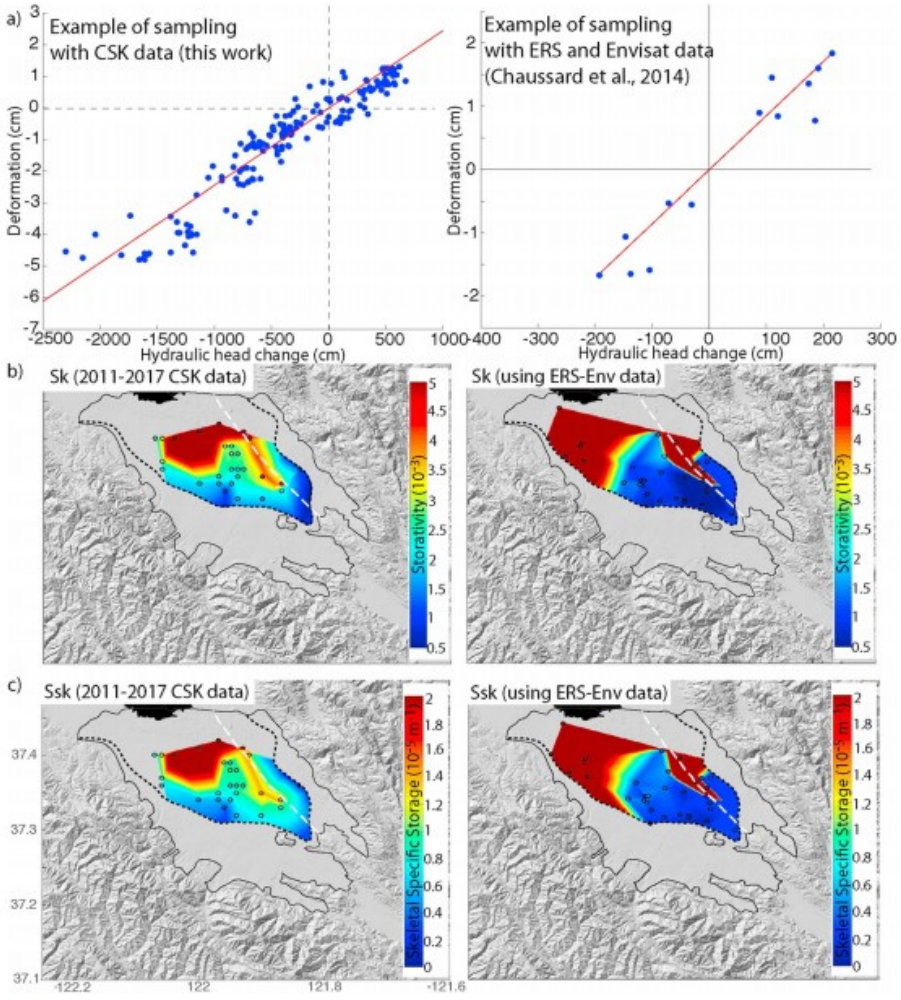

Figure 7. (a) Example of sampling (left) from CSK 2011–2017 and (right) from ERS and Envisat 1992–2011 for different wells in the Santa Clara Valley. The slope of the best fit linear regression between the deformation and the hydraulic head change corresponds to the Storativity (Sk). (b, left) Storativity (Sk) values derived from the CSK deformation and the 2011–2017 well data compared to the (right) storativity estimated from the ERS and Envisat data at the same scale, modified from Chaussard, Burgmann, et al. (2014). (c, left) Specific skeletal storage (Ssk) for CSK data compared to the (right) Ssk estimated from the ERS and Envisat data. Ssk is equal to Sk divided by the thickness of the saturated aquifer system.

We obtain similar results in the analyses for the three different time spans in the CSK data set (Figure S2), suggesting that the drought did not result in inelastic changes to the aquifer system. Figure 7b shows the Sk and Ssk values obtained with our 2011–2017 analysis (left) compared with the values obtained by Chaussard, Burgmann et al. (2014) with 1992–2011 data, shown with the same scale. The maximum uncertainties of the Sk values are of 10^{-3} and of 0.2×10^{-5} for the Ssk. While some differences are evident, no large

changes are detected. Both analyses suggest large Sk and Ssk values near the coast, in the Bay mud deposits known to be rich in clays (Borcherdt, 1970), and near the SCF where clays had also been suggested to explain the seasonal deformation partitioning (Chaussard, Burgmann et al., 2014). The main differences observed are smaller Sk and Ssk values near the SCF and larger values in the center of the confined aquifer. These differences are likely due to the different spatial sampling of the well data used and the increased temporal sampling of the CSK time series which leads to better constraints and confidence in the resulting properties (Figure 7a).

6 Water Storage and Load Changes

We use the water well data together with the surface deformation measurements, which provide constraints on water-level changes between the wells and enables interpolation (Chaussard, Burgmann et al., 2014), to evaluate the load changes associated with water storage fluctuations in the valley. Crustal deformation due to load changes from fluctuations in surface water and snow loads has been detected with GPS (Amos et al., 2014; Borsa, Agnew, & Cayan, 2014) and appears to influence microseismicity (Amos et al., 2014). However, local load changes, such as the ones in aquifer systems, are poorly resolved in regional models (Amos et al., 2014) as GPS stations are widely spaced and sites located in the aquifer cannot be used to constrain the elastic surface water load deformation.

We consider the water mass change as the product of the effective porosity and the water-level change (Bear, 2013). In the unconfined aquifer, the porosity is comparable to the storativity, which is approximately equal to the specific yield (Sy) (drainable porosity) (Ferris et al., 1962). The specific yield in the SCV has been previously estimated as being 0.02 for clay layers and 0.1 for sand-gravel layers (Hanson, Li, & Faunt, 2004; Johnson, 1967). The sand-gravel layers constitute the majority of the aquifer thickness in the unconfined aquifer; therefore, we use a specific yield of 0.1 for the unconfined aquifer, which is an upper bound. In the confined aquifer, the effective porosity comes from consolidation tests of cores. Newhouse et al. (2004) showed that the effective porosity in the SCV confined aquifer ranges from 0.2 to 0.4 for different depths. We use a mean effective porosity of 0.3 in the confined aquifer and estimate the storage and load changes for different time periods defined as follows: four load increase periods (water-level rise) in winter 2011 (September 2011 to April 2012), 2012 (October 2012 to February 2013), 2013 (September 2013 to February 2014), and from mid-2014 (August) to 2017 and three load decrease periods (drop in water levels) in summer 2012 (April to October), 2013 (February to September), and 2014 (February to August). For these periods, peak-to-peak values of the water levels (Δ_h) are used and the deformation is used to guide the spatial interpolation between wells (Chaussard, Burgmann, et al., 2014). These load changes are equivalent to the equivalent water thickness used by geodetic surveys (e.g., Amos et al., 2014; Famiglietti et al., 2011), which is the thickness of a layer of water that must be added or removed to account for

the observed changes in gravity. In the confined aquifer the water released or taken into storage comes from aquifer skeleton compression and water expansion rather than gravity drainage.

Figure 8 shows that the storage and load changes (top three rows) are limited to the confined aquifer and west of the SCF. The winter load increase (red, rise in water levels) is smaller than the summer load decrease (blue), each year between 2011 and 2014. A large load decrease (drop in water levels) is observed between winter 2011 and summer 2014, corresponding to a total loss in water storage of ~0.09 km^3 during the drought (Figure 8, bottom row). The post-2015 storage and load increase due to water-level recovery is of similar extent and amplitude as the drought-induced decrease. These observations confirm that the confined aquifer was the most affected by the drought because of increased pumping compared to the unconfined aquifer and that the drought led to only elastic load changes in the SCV. Water conservation and recharge efforts (see section 7) led to a rebound of the aquifer starting in late 2014, during the 2012–2015 drought period, and the aquifer had fully recovered by 2017.

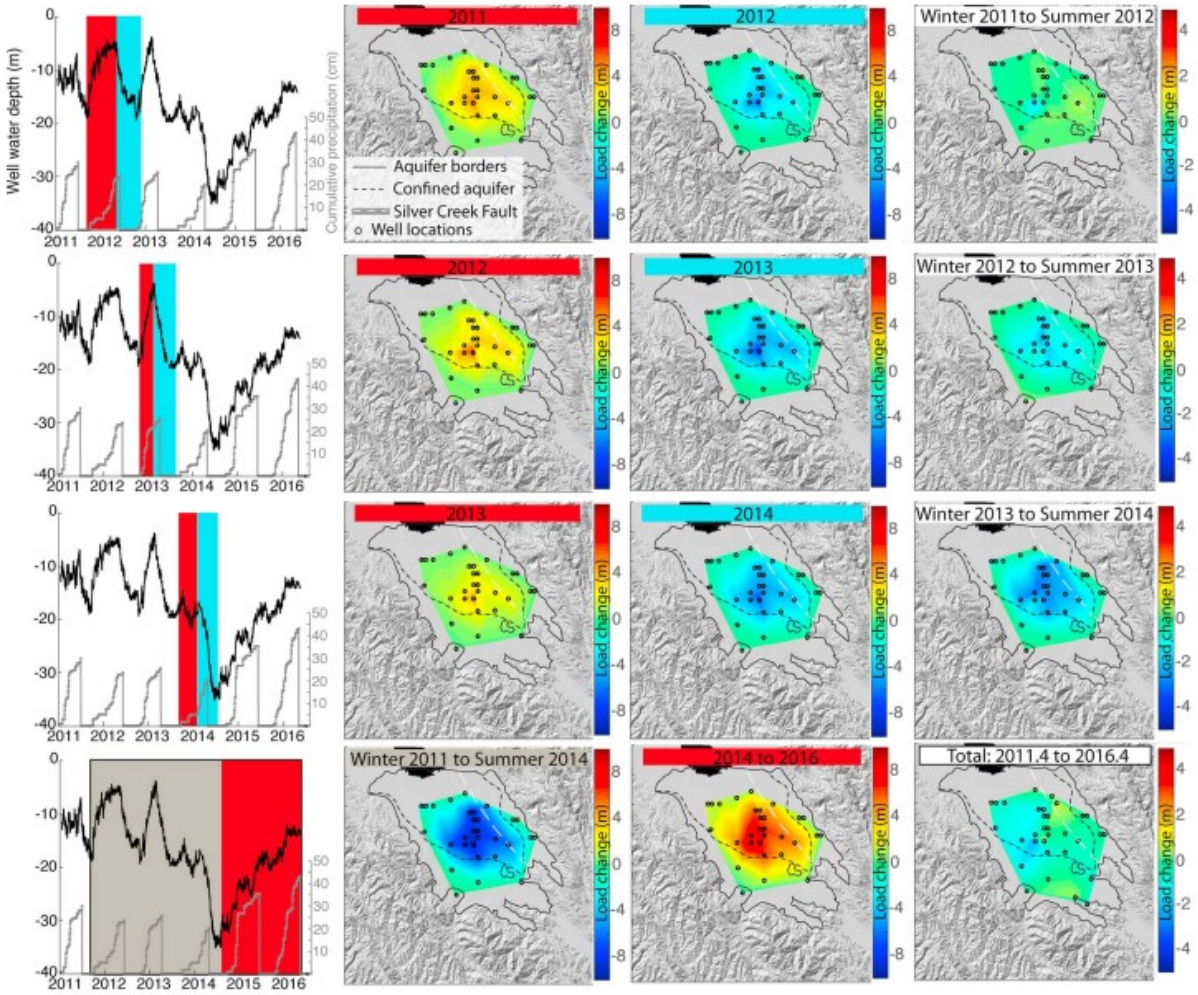

Figure 8. Interpolated seasonal load changes (expressed as equivalent water height changes) derived from 2011–2017 well data in the Santa Clara Valley. (left) The plots show the depth to water level for the well shown in Figure 4b (black) and precipitation (gray). The time span covered by the maps on the same row are highlighted in colors: red shades correspond to the increases in water levels (winter), blue shades correspond to the decreases in water levels (summer), and the gray shade on the last row correspond to the winter 2011 to summer 2014. The last column shows the net yearly change for the top three rows and the total change between mid-2011 and mid-2016 in the last row. Load changes are limited to the confined aquifer and west of the SCF, and a large load decrease is observed between winter 2012 and summer 2014 (last column, rows 2 and 3). The post-2015 load increase due to water-level recovery is of similar extent and amplitude as the drought-induced decrease (last row), suggesting elastic changes.

7 Discussion

In the unconfined aquifer, the deformation is of smaller amplitude and precisely tracks the water-level changes (Figure 4, bottom right). This agreement between the water-level changes and the elevation fluctuations suggests rapid infiltration of water and instantaneous equilibration with water levels (water table), which is consistent with the large hydraulic conductivity of aquifer layers. In contrast, in the center of the confined aquifer (Figure 4, top right) the deformation tracks the water levels prior to the drought, but a significant increase in subsidence is observed starting mid-2013 compared to the observed lowering of the water levels. This increased compaction is likely due to the effect of aquitard layers and reflects the difference in storativity and elastic skeletal specific storage of the confined aquifer. The elastic compressibility of aquitards is larger than

the elastic compressibility of aquifer layers by about 1 order of magnitude (Pavelko, 2004; Riley, 1998). Therefore, aquitard layers of the confined aquifer likely experience more compaction than aquifer layers even in the elastic domain of deformation. Thus, the amplified subsidence during the drought compared to the water-level drops, observed only in the confined aquifer, illustrates the higher elastic compressibility of aquitards compared to aquifers.

The time lag observed between water levels and deformation in the confined aquifer (Figure 5b) also suggests a role of the aquitard layers. Aquitard layers have a low hydraulic conductivity compared to aquifer layers, resulting in a slower equilibration with water levels. This results in a delayed poroelastic deformation observed both in the cross-correlation analysis (Figure 5b) and in the lag between water-level rise and uplift (Figure 4). Both of these characteristics, the large elastic compressibility and low hydraulic conductivity of aquitards compared to aquifer layers, explain the delayed recovery of the elevation compared to the water levels in the confined aquifer without requiring inelastic deformation.

The ICA efficiently isolates deformation patterns embedded in the long-term time series with less bias than PCA, as no orthogonality between the components is imposed. However, the ICA requires independent information to constrain the number of IC to extract. Therefore, PCA can be used to inform ICA. The ICA applied to the 2011–2017 SCV deformation reveals two signals of interest. First, the IC2 shows that the long-term uplift of the Evergreen Basin previously detected by Schmidt and Burgmann (2003) and Chaussard, Burgmann, et al. (2014) continued despite the drought. The uplift rate is of similar amplitude (~1 mm/yr) as the one constrained by Chaussard, Burgmann, et al. (2014) between 2000 and 2011. This prolonged uplift is made possible by the fact that the drought mostly affected the confined aquifer west of the SCF. Therefore, the continuing long-term poroelastic rebound due to the slow recovery of earlier aquitard compaction and relatively modest pumping of the aquifer system in the Evergreen Basin was unchanged during the drought.

The second pattern of interest isolated by the ICA is IC3 and the fact that IC3 is uncorrelated with IC1 starting mid-2013. IC3 captures a faster response of deformation near the SCF than in the rest of the confined aquifer controlled by precipitation (IC3 peaks occur at the onset of rainfall). The positive correlation between IC1 and IC3 between 2011 and 2013 reflects that the deformation in the aquifer system was regulated by precipitation recharge at that time. However, the anticorrelation between IC1 and IC3 after 2013 reflects that deformation in the aquifer system was regulated by pumping and imports rather than precipitation, and only the near SCF response captured by IC3 remained controlled by precipitation (Santa Clara Valley Water District, 2016).

The faster deformation near the SCF could be associated with a high vertical hydraulic conductivity near the fault, leading to increased along-fault flow, often described in fault damage zones due to the presence of fracture zones (Bense et al., 2013; Caine, Evans, & Forster, 1996). This high vertical hydraulic conductivity in the SCF does not preclude the low horizontal hydraulic conductivity of the fault demonstrated by Chaussard, Burgmann, et al. (2014), which effectively stops across-fault fluid flow and is likely due to clay smearing in the fault core (e.g., Bense, Van den Berg, & Van Balen, 2003; Knipe, 1993; Lindsay, Murphy, & Walsh, 1993; Lehner & Pilaar, 1991; Smith, 1980). Our observations suggest that the SCF is both a barrier to across-fault fluid flow and a conduit to along-fault flow.

The quantification of aquifer properties before and during the drought show no substantial change, suggesting that no inelastic deformation occurred in the SCV during the drought. Comparison of the 2011–2017 depth to water levels to data since 1915 (Figure 9) for a well in the center of the confined aquifer shows that the lowest water level experienced during the drought (~36 m) is significantly shallower than the lowest level experienced in 1964 (~72 m). This observation confirms that all the deformation in the SCV during the drought remained elastic. The lowest level experienced during the 2012–2015 drought is of similar amplitude as the ones of the 1934–1936 and 1988 lowstands.

Figure 9. Yearly depths to water level in the Santa Clara Valley since 1915 for a well near the extensometer MARTHA (Figure 4b). The blue line shows the daily data for the time period of observation (2011–2017). The minimum water level observed in the drought (~36 m) is shown with the dashed line and is approximately equal to the level observed in 1988 (depth to water level of 33 m) and in 1934–1936 (depth to water level of 36 m).

InSAR data can be used to determine basin-wide aquifer properties and their change in time, which provides an alternative method to meet the requirements of the Sustainable Groundwater Management Act that advocates for monitoring of all aquifers in the state of California (Moran & Cravens, 2015). The sole limitation of this technique for continuous monitoring of the SCV is InSAR data accessibility, as monitoring has been demonstrated for over 25 years with X, C, and L band data through this study and the work of Chaussard, Burgmann, et al. (2014). Applicability to other regions will depend on both data availability and noise contributions, especially in the form of decorrelation associated with seasonal vegetation changes. The SCV is highly urbanized, which leads to continuous correlation

and low noise levels. In contrast, the agricultural areas of California's Central Valley are highly vegetated with significant seasonal changes in land cover. L band InSAR has been shown to successfully enable continuous monitoring over vegetated areas (e.g., Chaussard et al., 2013; Chaussard, Wdowinski et al., 2014) but the long repeat intervals of existing data sets (ALOS 1 and 2) limit resolution. C band data have also shown promising results (e.g., Farr, 2016; Reeves et al., 2014) and with the increasing number of SAR systems, such as the European Satellite Agency's Sentinel-1 constellation, monitoring similar to the one of the SCV will become increasingly successful.

The water management practices of the SCV water district ensured that the aquifer system did not suffer from permanent loss of porosity associated with the drought. The recovery period started at the end of summer 2014 (August to September) before the onset of precipitation. It was achieved through reduced groundwater pumping and increased water import. In 2015 water pumping was reduced ~42% compared to 2014 and 27% compared to 2013 (Santa Clara Valley Water District, 2016; V. De La Piedra, personal communications, 2017). Limits were set on days for outdoor irrigation, a large outreach campaign was deployed to encourage reduced water usage, and the SCV water district invested in efficient irrigation equipment and turf replacement. Additionally, due to the very limited local supplies, over 80% of the recharge in the SCV was from imported water in 2015. The 2015 managed recharge (0.068 km^3) was almost tripled compared to 2014 (Santa Clara Valley Water District, 2016). The total recharge in 2015 reached 0.12 km^3, ~43% of the groundwater storage at the end of the year. Import of surface water was used for direct recharge, as well as supplemental supplies through exchanges and transfers, and treated and recycled water was used for irrigation. Such conservation programs, outreach efforts, and water imports cost the SCV water district $18.9 million in 2015. These response activities were extremely successful and ensured rapid recovery and no permanent damage to the aquifer system.

The storage and load change analysis reveals that the loads experienced by the SCV are large, on the order of meters of equivalent water thickness. Before the drought ~4 m of seasonal load change was observed, approximately canceling out at the end of each year. During the drought and subsequent recovery, load changes were on the order of ~6 m, fully recovering by mid-2016. The equivalent total water volume loss between 2011 and the peak drawdown in 2014 is about ~0.09 km^3 while seasonal load change prior to the drought are on the order of ~0.02 km^3. These large load changes are due to the combined effects of the large well-level fluctuations, the significant thickness of the aquifer and aquitard layers, and the large effective porosity of the basin, especially in the confined aquifer. The dimensions (~10 km across) and amplitude (several meters) of equivalent water height changes involved suggest that the SCV load changes are comparable to that of some of California's reservoirs (e.g., Argus, Fu, & Landerer, 2014; Wahr et al., 2013). For comparison, Shasta Lake level

changes can reach 20 m, with a comparable surface area. Such large load changes are nonnegligible even if local and should therefore be integrated into large-scale models as they could influence the seismicity on nearby active faults. The SCV confined aquifer is as close as ~10 km east of the San Andreas Fault and ~7 km west of the Hayward-Calaveras fault zone (Chaussard, Burgmann, Fattahi, Johnson, et al., 2015; Chaussard, Burgmann, Fattahi, Nadeau, et al., 2015), but as the aquifer extent is small, it leads to only minimal load changes. However, in the San Joaquin Valley, given the significantly larger spatial extent of the load (~40 times the area of the SCV) and the much larger load fluctuations induced by prolonged groundwater withdrawal (Farr et al., 2016), aquifer load changes may play a role on the stress fluctuations of the San Andreas Fault system, as close as ~15 km to the west. Load changes in the Central Valley have been estimated in the regional GPS-derived model, but only stations outside of the valley are used to estimate the load distribution and the Gravity Recovery and Climate Experiment (GRACE)'s resolution of 300–500 km is too coarse. Therefore, a full InSAR-GPS-GRACE integration should be used to address this problem.

8 Conclusions

The 2011–2017 COSMO-SkyMed InSAR time series analysis of surface deformation over the SCV aquifer demonstrates that remotely sensed deformation with a high temporal sampling can be used to track water through an aquifer system, improves groundwater monitoring and aquifer characterization, and allows us to assess the success of water management practices. In the SCV, the confined aquifer was the most affected by the 2012–2015 drought due to pumping, with minimum water levels and surface elevations reached by summer 2014. Thanks to a substantial effort of the water district to reduce water pumping, through conservation programs and outreach efforts, and to increase water imports and managed recharge of the aquifer, the drought did not lead to irreversible changes of the aquifer system. By 2017, water levels were back to their predrought levels, while the surface elevation had not yet fully recovered due to the delayed poroelastic response of aquitards and their amplified elastic compressibility. Analysis of predrought and during-drought storativity and load changes confirms that the drought led to only elastic changes in the SCV, demonstrating that InSAR time series can be used to assess the “health” of aquifers and track changes in water storage. Finally, this work also shows that seasonal water mass and load changes associated with aquifer systems can be large, suggesting that even localized drawdowns can influence regional stress and may be able to affect seismicity rates. Worldwide InSAR monitoring of aquifers can help water management efforts and ensure sustainability of precious global groundwater resources.

Acknowledgments

We thank the Italian Space Agency (ASI) for providing the COSMO-SkyMed data for this project. Original COSMO-SkyMed products are copyrighted by

the Agenzia Spaziale Italiana (2008–2017). We are very grateful to the Santa Clara Valley Water District, especially Vanessa De La Piedra, for sharing the data and drought mitigation effort information with us. The Santa Clara Valley Water District data used in this paper can be obtained upon request through the following link: http://www.valleywater.org/PublicRecords.aspx. The InSAR time series products are accessible as supporting information. E.C. and R.B. thank the National Aeronautics and Space Administration (NASA) for the support through grant NNX12AQ32G. P.M. thanks NASA for the sponsor through the NASA Postdoctoral program administered by the University Space Research Association (USRA). The authors also thank one anonymous reviewer, Tom Farr, and the Associate Editor, Emma Hill, for their constructive comments that helped significantly improve the quality of the manuscript.

References

Amos, C. B., Audet, P., Hammond, W. C., Burgmann, R., Johanson, I. A., & Blewitt, G. (2014). Uplift and seismicity driven by groundwater depletion in central California. *Nature*, 509(7501), 483– 486. https://doi.org/10.1038/nature13275

Argus, D. F., Fu, Y., & Landerer, F. W. (2014). Seasonal variation in total water storage in California inferred from GPS observations of vertical land motion. *Geophysical Research Letters*, 41, 1971– 1980. https://doi.org/10.1002/2014GL059570

Bear, J. (2013). Dynamics of fluids in porous media. (pp. 800). Courier Corporation, Technology & Engineering.

Bell, J. W., Amelung, F., Ferretti, A., Bianchi, M., & Novali, F. (2008). Permanent scatterer InSAR reveals seasonal and long-term aquifer-system response to groundwater pumping and artificial recharge. *Water Resources Research*, 44, W02407. https://doi.org/10.1029/2007WR006152

Bense, V. F., Gleeson, T., Loveless, S. E., Bour, O., & Scibek, J. (2013). Fault zone hydrogeology. *Earth Science Review*, 127, 1– 22. https://doi.org/10.1016/j.earscirev.2013.09.008

Bense, V. F., Van den Berg, E. H., & Van Balen, R. T. (2003). Deformation mechanisms and hydraulic properties of fault zones in unconsolidated sediments; the Roer Valley Rift System, the Netherlands. *Hydrogeology Journal*, 11(3), 319– 332. https://doi.org/10.1007/s10040-003-0262-8

Borcherdt, R. D. (1970). Effects of local geology on ground motion near San Francisco Bay. *Bulletin of the Seismological Society of America*, 60(1), 29–61.

Borsa, A. A., Agnew, D. C., & Cayan, D. R. (2014). Ongoing drought-induced uplift in the western United States. *Science*, 345(6204), 1587– 1590. https://doi.org/10.1126/science.1260279

Burbey, T. J. (2001). Stress-strain analyses for aquifer-system characterization. *Ground Water*, 39(1), 128– 136.

Burgmann, R., Rosen, P. A., & Fielding, E. J. (2000). Synthetic aperture radar interferometry to measure Earth's surface topography and its deformation. *Annual Review Earth and Planetary Science*, 28(1), 169– 209.

Caine, J. S., Evans, J. P., & Forster, C. B. (1996). Fault zone architecture and permeability structure. *Geolgy*, 24, 1025– 1028.

Chaussard, E., Amelung, F., Abidin, H., & Hong, S.-H. (2013). Sinking cities in Indonesia: ALOS PALSAR detects rapid subsidence due to groundwater and gas extraction. *Remote Sensing of Environment*, 128, 150– 161. https://doi.org/10.1016/j.rse.2012.10.015

Chaussard, E., Burgmann, R., Fattahi, H., Johnson, C. W., Nadeau, R. M., Taira, T., & Johanson, I. (2015). Interseismic coupling and refined earthquake potential on the Hayward-Calaveras fault zone. *Journal of Geophysical Research: Solid Earth*, 120, 8570– 8590. https://doi.org/10.1002/(ISSN)2169-9356

Chaussard, E., Burgmann, R., Fattahi, H., Nadeau, R. M. M., Taira, T., Johnson, C. W., & Johanson, I. (2015). Potential for larger earthquakes in the East San Francisco Bay Area due to the direct connection between the Hayward and Calaveras Faults. *Geophysical Research Letters*, 42, 2734– 2741. https://doi.org/10.1002/2015GL063575

Chaussard, E., Burgmann, R., Shirzaei, M., Fielding, E. J., & Baker, B. (2014). Predictability of hydraulic head changes and characterization of aquifer-system and fault properties from InSAR-derived ground deformation. *Journal of Geophysical Research: Solid Earth*, 119, 6572– 6590. https://doi.org/10.1002/2014JB011266

Chaussard, E., Wdowinski, S., Cabral-Cano, E., & Amelung, F. (2014). Land subsidence in central Mexico detected by ALOS InSAR time-series. *Remote Sensing of Environment*, 140, 94– 106. https://doi.org/10.1016/j.rse.2013.08.038

Colesanti, C., Ferretti, A., Novali, F., Prati, C., & Rocca, F. (2003). SAR monitoring of progressive and seasonal ground deformation using the permanent scatterers technique. *IEEE Transactions on Geoscience and Remote Sensing*, 41(7), 1685– 1701. https://doi.org/10.1109/TGRS.2003.813278

Costa-Cabral, M., Rath, J. S., Mills, W. B., Roy, S. B., Bromirski, P. D., & Milesi, C. (2016). Projecting and forecasting winter precipitation extremes and meteorological drought in California using the North Pacific high sea level pressure anomaly. *Journal of Climate*, 29(13), 5009– 5026.

Famiglietti, J. S., Lo, M., Ho, S. L., Bethune, J., Anderson, K. J., Syed, T. H., … Rodell, M. (2011). Satellites measure recent rates of groundwater depletion

in California's Central Valley. *Geophysical Research Letters*, 38. L03403. https://doi.org/10.1029/2010GL046442

Farr, T. G. (2016). InSAR measurements of subsidence in the Central Valley, California from 2007–present, *EUSAR 2016: 11th European Conference on Synthetic Aperture Radar*, VDE, Hamburg, Germany. https://doi.org/10.1029/2010WR010312

Farr, T. G., Jones, C. E., & Liu, Z. (2016). Progress report: Subsidence in California, March 2015–September 2016. *NASA Progress Report;* http://www.water.ca.gov/waterconditions/docs/2017/JPL%20subsidence%20report%20final%20for%20public%20dec%202016.pdf

Ferretti, A., Prati, C., & Rocca, F. (2000). Nonlinear subsidence rate estimation using permanent scatterers in differential SAR interferometry. *IEEE Transactions on Geoscience and Remote Sensing*, 38(5), 2202– 2212. https://doi.org/10.1109/36.868878

Ferretti, A., Prati, C., & Rocca, F. (2001). Permanent scatterers in SAR interferometry. *IEEE Transactions Geoscience Remote Sensing*, 39(1), 8– 20. https://doi.org/10.1109/36.898661

Ferris, J. G., Knowles, D. B., Brown, R. H., & Stallman, R. W. (1962). Theory of aquifer tests, U.S. Geological Survey Water-Supply Paper 1536 E, 174 p.

Fielding, E. J., Simons, M., Owen, S., Lundgren, P., Hua, H., Agram, P., … Samsonov, S. (2014). Rapid imaging of earthquake ruptures with combined geodetic and seismic analysis. *Procedia Technology*, 16, 876– 885.

Freeze, R. A., & Cherry, J. A. (1979). *Groundwater*. Englewood Cliffs, NJ: Prentice-Hall.

Galloway, D. L., & Hoffmann, J. (2006). The application of satellite differential SAR interferometry-derived ground displacements in hydrogeology. *Hydrogeology Journal*, 15(1), 133– 154. https://doi.org/10.1007/s10040-006-0121-5

Hanson, R. T., Li, Z., & Faunt, C. (2004). Documentation of the Santa Clara Valley regional ground-water/surface-water flow model, Santa Clara Valley, California, U.S. Geological Survey Science Investment Representative.

Helm, D. C. (1976). Estimating parameters of compacting fine-grained interbeds within a confined aquifer system by a one-dimensional simulation of field observations. *International Association of Hydrological Sciences Proceedings of the Anaheim Symposium*, 1976(121), 145– 156.

Hoffmann, J., Zebker, H. A., Galloway, D. L., & Amelung, F. (2001). Seasonal subsidence and rebound in Las Vegas Valley, Nevada, observed by synthetic aperture radar interferometry. *Water Resources Research*, 37, 1551– 1566.

Hyvärinen, A., & Oja, E. (1997). A fast fixed-point algorithm for independent component analysis. *Neural Computation*, 9(7), 1483– 1492.

Hyvärinen, A., Karhunen, J., & Oja, E. (2004). *Independent Component Analysis*. Hoboken, NJ: John Wiley, 2001.

Jarvis, A., Reuter, H. I., Nelson, A., & Guevara, E. (2008). Hole-filled seamless SRTM data v4, International Centre for Tropical Agriculture (CIAT). Retrieve from http://srtm.csi.cgiar.org

Johnson, A. I. (1967). *Specific yield: Compilation of specific yields for various materials*. (pp. 74). U.S. Geological Survey Water Supply Paper 1662-D. Washington, DC.

Knipe, R. J. (1993). The influence of fault zone processes and diagenesis on fluid flow. *Diagenesis and Basin Development, Studies Geological Series*, 36, 135– 148.

Koltermann, C. E., & Gorelick, S. M. (1992). Paleoclimatic signature in terrestrial flood deposits. *Science*, 256(5065), 1775– 1782. https://doi.org/10.1126/science.256.5065.1775

Lehner, F. K., & Pilaar, W. F. (1991). On a mechanism of clay smear emplacement in synsedimentary normal faults. In P. Møller-Pedersen, & A. G. Koestler (Eds.), *Hydrocarbon Seals: Importance for Exploration and Production* NPF Spec. Publ., (Vol. 7, pp. 39– 50). New York: Elsevier.

Lindsay, N. G., Murphy, F. C., & Walsh, J. J. (1993). Outcrop studies of shale smears on fault surfaces. In S. S. Flint, & I. D. Bryant (Eds.), *The Geological Modelling of Hydrocarbon Reservoirs and Outcrop Analogues* (Vol. 15, pp. 113– 123). Oxford, UK: Blackwell Publishing Ltd. https://doi.org/10.1002/9781444303957.ch6

Massonnet, D., Rossi, M., Carmona, C., Adragna, F., Peltzer, G., Feigl, K. L., & Rabaute, T. (1993). The displacement field of the Landers earthquake mapped by radar interferometry. *Nature*, 364, 138– 142.

Milillo, P., Bürgmann, R., Lundgren, P., Salzer, J., Perissin, D., Fielding, E., … Milillo, G. (2016). Space geodetic monitoring of engineered structures: The ongoing destabilization of the Mosul dam, Iraq. *Scientific Reports*, *6*.

Milillo, P., Riel, B., Minchew, B., Yun, S. H., Simons, M., & Lundgren, P. (2016). On the synergistic use of SAR constellations' data exploitation for Earth science and natural hazard response. *IEEE Journal of Selected Topics in Applied Earth Observations and Remote Sensing*, 9(3), 1095– 1100.

Moran, T., & Cravens, A. (2015). California's Sustainable Groundwater Management Act of 2014: Recommendations for preventing and resolving groundwater conflicts.

Newhouse, M. W., Hanson, R. T., Wentworth, C. M., Everett, R. R., Williams, C. F., Tinsley, J. C., … Carkin, B. A. (2004). Geologic, water-chemistry, and hydrologic data from multiple-well monitoring sites and selected water-supply wells in the Santa Clara Valley, California, 1999–2003, *U.S. Geological Survey Science Investment Representative 2004–5250,* 142 p.

Oja, E. (1982). Simplified neuron model as a principal component analyzer. *Journal of Mathematical Biology*, 15(3), 267– 273.

Pavelko, M. T. (2004). Estimates of hydraulic properties from a one-dimensional numerical model of vertical aquifer-system deformation, Lorenzi Site, Las Vegas, Nevada, *U.S. Geological Survey*. *Water-Resources Investigations Report 03–4083*, 1– 45.

Perissin, D., Wang, Z., & Wang, T. (2011). The SARPROZ InSAR tool for urban subsidence/manmade structure stability monitoring in China. *Proceedings of the ISRSE, Sidney, Australia, 1015*.

Poland, J. F., & Ireland, R. L. (1988). Land subsidence in the Santa Clara Valley, California, as of 1982, *Mechanics of Aquifer Systems, U.S. Geological Survey Professional Paper, 497-F*, 61 pp.

Reeves, J. A., Knight, R., Zebker, H. A., Kitanidis, P. K., & Schreüder, W. A. (2014). Estimating temporal changes in hydraulic head using InSAR data in the San Luis Valley, Colorado. *Water Resources Research*, 50, 4459– 4473. https://doi.org/10.1002/2013WR014938

Reimann, C., Filzmoser, P., Garrett, R. G., & Dutter, R. (2008). Principal component analysis (PCA) and factor analysis (FA). *Statistical data analysis explained: Applied environmental statistics with R*, 211–232.

Riley, F. S. (1998). Mechanics of aquifer systems—The scientific legacy of Joseph F. Poland, in Land Subsidence: Case studies and current research, Proceedings of the Dr. Joseph F. Poland Symposium on Land Subsidence, Assoc. Eng. Geol. Spec. Publ., vol. 8, edited by J. W. Borchers, pp. 13– 27, Sacramento, CA, Star, Belmont, CA.

Robeson, S. M. (2015). Revisiting the recent California drought as an extreme value. *Geophysical Research Letters*, 42, 6771– 6779. https://doi.org/10.1002/2015GL064593.

Rosen, P. A., Hensley, S., Joughin, I. R., Li, F. K., Madsen, S. N., Rodriguez, E., & Goldstein, R. M. (2000). Synthetic aperture radar interferometry. *Proceedings of the IEEE*, 88(3), 333– 382. https://doi.org/10.1109/5.838084

Santa Clara Valley Water District (2016). Protection and augmentation of water supplies 2016–2017, *45th Annual Report,* Santa Clara Valley Water District.

Schmidt, D. A., & Burgmann, R. (2003). Time-dependent land uplift and subsidence in the Santa Clara Valley, California, from a large interferometric synthetic aperture radar data set. *Journal of Geophysical Research*, 108(B9), 2416. https://doi.org/10.1029/2002JB002267

Shah, T. (2005). Groundwater and human development: challenges and opportunities in livelihoods and environment. *Water Science and Technology*, 51(8), 27– 37.

Smith, D. A. (1980). Sealing and nonsealing faults in Louisiana Gulf Coast salt basin. *American Association of Petroleum Geologists Bulletin*, 64, 145– 152.

Swain, D. L. (2015). A tale of two California droughts: Lessons amidst record warmth and dryness in a region of complex physical and human geography. *Geophysical Research Letters*, 42, 2734– 2741. https://doi.org/10.1002/2015GL06662

Tolman, C. F., & Poland, J. F. (1940). Ground-water, salt-water infiltration, and ground-surface recession in Santa Clara Valley, Santa Clara County, California. *Transactions American Geophysical Union*, 21(1), 23. https://doi.org/10.1029/TR021i001p00023

Wahr, J., Khan, S. A., van Dam, T., Liu, L., van Angelen, J. H., van den Broeke, M. R., & Meertens, C. M. (2013). The use of GPS horizontals for loading studies, with applications to Northern California and southeast Greenland. *Journal of Geophysical Research: Solid Earth*, 118, 1795– 1806. https://doi.org/10.1002/jgrb.50104

Wentworth, C. M., Williams, R. A., Jachens, R. C., Graymer, R. W., & Stephenson, W. J. (2010). The Quaternary Silver Creek Fault beneath the Santa Clara Valley, California. *U.S. Geological Survey Open File Representative, 2010–1010*.

Wilson, A. M., & Gorelick, S. (1996). The effects of pulsed pumping on land subsidence in the Santa Clara Valley, California. *Journal of Hydrology*, 174(3), 375– 396.

Wright, T. J., Parsons, B. E., & Lu, Z. (2004). Toward mapping surface deformation in three dimensions using InSAR. *Geophysical Research Letters*, 31, L01607. https://doi.org/10.1029/2003GL018827